J. Fluid Mech. (2010), *vol.* 659, *pp.* 405–419.
doi:10.1017/S0022112010002557

On the near-wall characteristics of acceleration in turbulence

K. YEO[1]†, B.-G. KIM[2] AND C. LEE[1,2]‡

[1]Department of Mechanical Engineering, Yonsei University, Seoul 120–749, Korea

[2]Department of Computational Science and Engineering, Yonsei University, Seoul 120–749, Korea

(Received 29 January 2010; revised 26 April 2010; accepted 26 April 2010;
first published online 23 July 2010)

The behaviour of fluid-particle acceleration in near-wall turbulent flows is investigated in numerically simulated turbulent channel flows at low to moderate Reynolds numbers, $Re_\tau = 180 \sim 600$. The acceleration is decomposed into pressure-gradient (irrotational) and viscous contributions (solenoidal acceleration) and the statistics of each component are analysed. In near-wall turbulent flows, the probability density function of acceleration is strongly dependent on the distance from the wall. Unexpectedly, the intermittency of acceleration is strongest in the viscous sublayer, where the acceleration flatness factor of $O(100)$ is observed. It is shown that the centripetal acceleration around coherent vortical structures is an important source of the acceleration intermittency. We found sheet-like structures of strong solenoidal accelerations near the wall, which are associated with the background shear modified by the interaction between a streamwise vortex and the wall. We found that the acceleration Kolmogorov constant is a linear function of y^+ in the log layer. The Reynolds number dependence of the acceleration statistics is investigated.

Key words: intermittency, turbulent boundary layers, turbulence simulation

1. Introduction

Lagrangian acceleration is one of the fundamental variables in the Navier–Stokes equations and of great importance in understanding Lagrangian nature of turbulent flows. The study on acceleration is relevant not only to theoretical developments (Hill 2002; Biferale *et al.* 2004; Yeung *et al.* 2007) but also to many engineering applications, such as the prediction of near-surface dispersion of airborne pollutant (Sawford 1991; Pope 1994; Reynolds 1999) and particle deposition onto a surface (Brooke *et al.* 1992; Setyawan *et al.* 2002). Because of the Lagrangian nature, measurement of acceleration is a challenging task and only quite recently have direct measurements of acceleration become possible using optical imaging (La Porta *et al.* 2001). Due to developments of experimental techniques and high-performance computing, fluid-particle acceleration has been studied extensively over the last decade (see Toschi & Bodenschatz 2009 for a review). Recently, acceleration of finite-sized and/or inertial particles has begun to attract considerable attention (Qureshi *et al.* 2007; Volk *et al.* 2008; Calzavarnini *et al.* 2009; Yeo *et al.* 2010). Now, there is a large volume of literature on the behaviour

† Present address: Division of Applied Mathematics, Brown University, Providence, RI 02912, USA

‡ Email address for correspondence: clee@yonsei.ac.kr

of acceleration in isotropic turbulence and our understanding of acceleration in isotropic turbulence is much more advanced than that in inhomogeneous turbulent flows, such as turbulent shear layers. Still, there are only a limited number of studies on the behaviour of acceleration in near-wall turbulence (Lee, Yeo & Choi 2004; Gerashchenko *et al.* 2008; Yeo, Kim & Lee 2009).

Monin & Yaglom (1975) suggested that the Lagrangian acceleration is largely determined by the smallest scale motion, smaller than the Kolmogorov scale, and pressure forces mainly contribute to the acceleration at high Reynolds numbers. Hill & Thoroddsen (1997) estimated the two-point correlation of acceleration from the third- and fourth-order velocity structure functions to show that the viscous-force contribution to acceleration is negligible compared to that of the pressure force. Yeung (1997) found in the simulation of homogeneous shear flow that the one- and two-particle correlations of acceleration exhibit an approximately isotropic behaviour, which is consistent with the local isotropy.

According to the classical Kolmogorov similarity theory, the acceleration Kolmogorov constant, acceleration variance scaled by ϵ and ν, is a universal constant at sufficiently high Reynolds number. However, it is still not clear whether the acceleration variance exhibits the universal behaviour at high Reynolds number. Yeung & Pope (1989) found in the simulation of isotropic turbulence that the acceleration Kolmogorov constant is not universal and rather increases as $Re_\lambda{}^{1/2}$, where Re_λ denotes the Taylor-scale Reynolds number. Vedula & Yeung (1999) suggested that the Reynolds number dependence comes from the non-universal behaviour of pressure-gradient statistics. Gotoh & Rogallo (1999) proposed a theoretical model which assumes that the small-scale pressure field is driven by coherent structures to explain the Reynolds number dependence of acceleration statistics. La Porta *et al.* (2001) showed that acceleration is highly intermittent in their direct measurement of the Lagrangian acceleration in quasi-isotropic turbulence. They claimed that the Kolmogorov scaling is attained at high Re_λ. Yeung *et al.* (2006) performed direct numerical simulations (DNS) of isotropic turbulence for $Re_\lambda = 40 \sim 680$ and suggested a fitting curve for the acceleration Kolmogorov constant. Recently, Gulitski *et al.* (2007) measured acceleration variances for Re_λ up to 10^4. They showed that the acceleration Kolmogorov constant depends on Re_λ even at $Re_\lambda \sim 10^4$ and the behaviour of the acceleration Kolmogorov constant is well predicted with the fitting curve by Yeung *et al.* (2006).

The Navier–Stokes equations relate the Lagrangian acceleration to the Eulerian variables (Monin & Yaglom 1975). The Lagrangian acceleration ($\boldsymbol{a}$) is composed of two contributions from the pressure-gradient and the viscous forces. Conventionally, the pressure-gradient force is called potential or irrotational acceleration ($\boldsymbol{a}^I$) and the viscous force is solenoidal acceleration ($\boldsymbol{a}^S$), owing to their inherent characteristics (Monin & Yaglom 1975; Vedula & Yeung 1999). It has been discussed in isotropic turbulence that $\boldsymbol{a}^I$ mainly contributes to $\boldsymbol{a}$ and the correlation between $\boldsymbol{a}$ and $\boldsymbol{a}^S$ becomes negligible as the Reynolds number increases (Hill & Thoroddsen 1997; Tsinober, Vedula & Yeung 2001). In near-wall turbulence, however, the turbulent field is highly anisotropic and the viscous effects become dominant in the vicinity of the wall. Therefore, the behaviour of acceleration may be different from that in isotropic turbulence.

The main purpose of this study is to investigate the behaviour of acceleration in near-wall turbulent flow. Particularly, we focus on the connection between near-wall coherent structures and acceleration. We performed DNS of turbulent channel flow at low to moderate Reynolds number. We report various acceleration statistics which

Re_τ	$N_x \times N_y \times N_z$	Δx^+	Δz^+	Δy^+_{min}
180	$192 \times 129 \times 192$	11.8	3.93	0.05
408	$192 \times 193 \times 192$	13.1	4.36	0.05
600	$320 \times 257 \times 320$	11.8	3.93	0.05

TABLE 1. Simulation parameters. $N_x \times N_y \times N_z$ are the number of modes and Δx^+, Δy^+ and Δz^+ are the numerical grid spacings normalized by the wall units in the streamwise, wall-normal and spanwise directions, respectively.

have not been presented for near-wall turbulence. The different behaviours of $\boldsymbol{a}$, $\boldsymbol{a}^I$ and $\boldsymbol{a}^S$ around the coherent structures are illustrated.

The remainder of this paper is organized as follows: numerical methods are briefly described in § 2; acceleration statistics are analysed in § 3; the behaviour of acceleration near a coherent structure is presented in § 4; finally, the conclusions are provided in § 5.

2. Numerical approach

The Navier–Stokes equations for incompressible flow are

$$\frac{\partial u_i}{\partial x_i} = 0, \tag{2.1}$$

$$\frac{\mathrm{D}u_i}{\mathrm{D}t} = -\frac{\partial p}{\partial x_i} + \frac{1}{Re_\tau}\nabla^2 u_i, \tag{2.2}$$

where x_1, x_2 and x_3 denote the streamwise (x), wall-normal (y) and spanwise directions (z), respectively. Here, the u_i are the corresponding velocity components (u, v, w), p is pressure and Re_τ is the Reynolds number based on the channel half-width δ and the wall-shear velocity u_τ. All variables in (2.1) and (2.2) are non-dimensionalized by δ and u_τ.

The acceleration fields are computed by DNS of turbulent channel flow at $Re_\tau = 180$, 408 and 600. The Navier–Stokes equations were solved by using a spectral method: dealiased Fourier and Chebyshev expansions are used in the horizontal and the wall-normal directions, respectively. The time advancement was carried out by employing the Crank–Nicolson scheme for the viscous terms and a third-order Runge–Kutta scheme for the nonlinear terms (Lundbladh *et al.* 1999). Periodic boundary conditions are used in the horizontal directions. The computational domain size and the grid sizes in wall units are listed in table 1.

A $128 \times 129 \times 128$ mesh has been used for DNS studies of turbulent channel flows at $Re_\tau = 180$ and shown to be sufficient to resolve the velocity statistics (Moser, Kim & Mansour 1999). However, as the fluid acceleration is highly intermittent, it may need a finer resolution to estimate the acceleration statistics accurately. Figure 1 shows the flatness factors of the spanwise acceleration F_z obtained for three different resolutions at $Re_\tau = 180$. It is observed that F_z is slightly underestimated when using the usual $128 \times 129 \times 128$ mesh. Therefore, we used a $192 \times 129 \times 192$ mesh for $Re_\tau = 180$ and the mesh sizes for higher Re_τ are determined to keep the same resolution in the wall units.

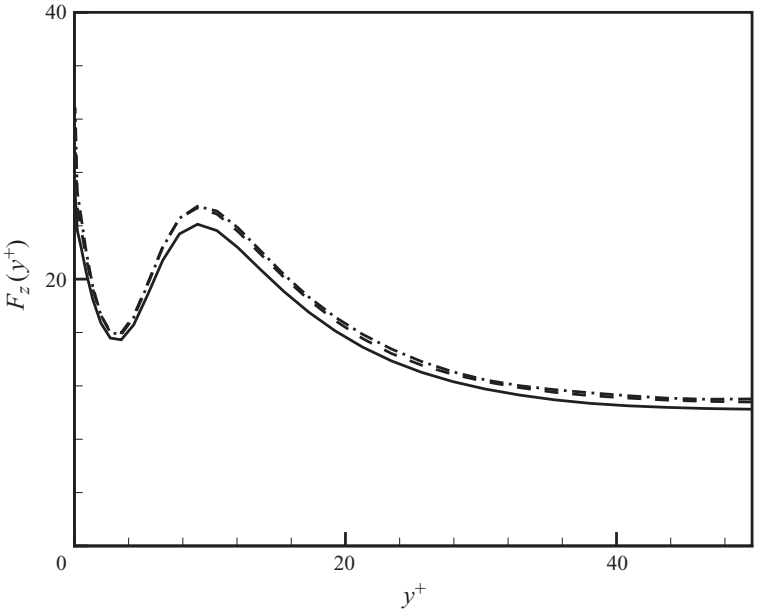

FIGURE 1. The flatness factors of the spanwise acceleration for different resolutions at $Re_\tau = 180$. Solid line, $128 \times 129 \times 128$; dashed line, $192 \times 129 \times 192$; dash-dot line, $256 \times 129 \times 258$.

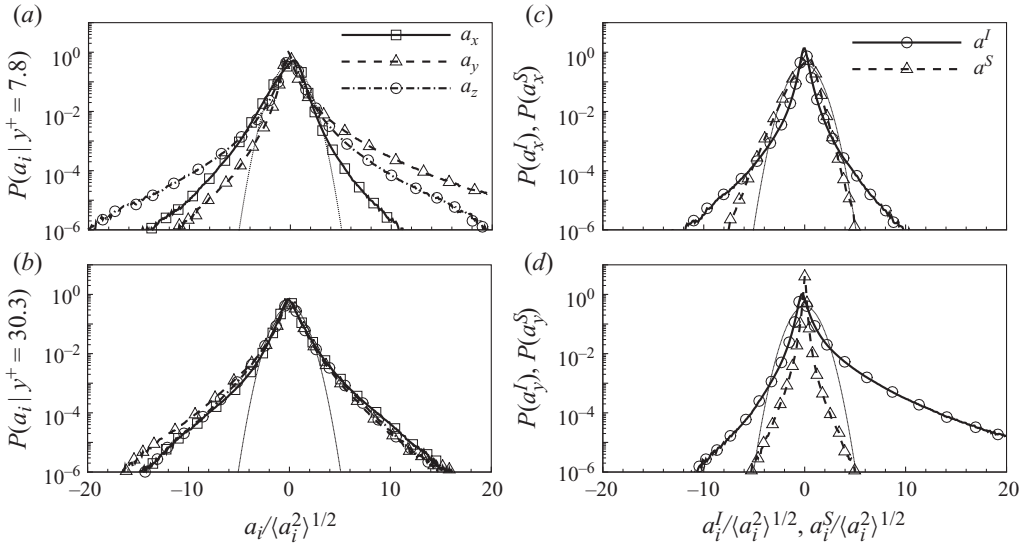

FIGURE 2. Probability density functions of acceleration fluctuations in (*a*) viscous ($y^+ = 7.8$) and (*b*) buffer layers ($y^+ = 30.3$) at $Re_\tau = 180$. (*c*) and (*d*) are, respectively, the p.d.f. of the streamwise and wall-normal components of a^I and a^S at $y^+ = 7.8$. All p.d.f.s are normalized by standard deviations of the total accelerations, $\langle a_i^2 \rangle^{1/2}$. The dotted lines in (*a*)–(*d*) are the Gaussian distribution.

3. Acceleration statistics

3.1. *Probability distribution of acceleration*

The probability density functions (p.d.f.) for acceleration fluctuations at different wall-normal distances for $Re_\tau = 180$ are shown in figure 2(*a*, *b*). Each p.d.f. is evaluated with

about 3.7×10^8 samples and normalized by the root-mean-square (r.m.s.) accelerations $\langle a_i'^2 \rangle^{1/2}$, where $\langle \cdot \rangle$ denotes ensemble average. Hereafter, we use lower-case characters to indicate fluctuating components and upper-case characters for mean components, unless mentioned otherwise. Consistently with the previous experiments (Voth *et al.* 2002) and DNS (Vedula & Yeung 1999) in isotropic turbulence, the acceleration p.d.f.s show long tails compared to that of the Gaussian distribution. Near the wall, the p.d.f.s of a_x and a_y are strongly skewed. The p.d.f. of a_x at $y^+ = 7.8$ is negatively skewed whereas that of a_y is positively skewed, in which the superscript $+$ denotes a variable normalized by the inner variables (u_τ and ν). The p.d.f.s become nearly symmetric at $y^+ = 30.3$. As expected, the p.d.f. of a_z is always symmetric regardless of the distance from the wall.

It is interesting to observe that the acceleration p.d.f.s in the viscous sublayer (figure 2*a*) show wider tails than those in the buffer layer (figure 2*b*). In the p.d.f. of a_y at $y^+ = 7.8$, extreme events, 50 times larger than the r.m.s. value, are observed with the probability of 10^{-7}. The maximum flatness factor of a_y is about 280 at $y^+ \simeq 5$ (figure 4*c*), which is much larger than the flatness factor observed in isotropic turbulence; about 90 for $Re_\lambda = 690$ (La Porta *et al.* 2001; Voth *et al.* 2002).

Acceleration in isotropic turbulence is dominated by the potential contribution $\boldsymbol{a}^I$ (Monin & Yaglom 1975; Vedula & Yeung 1999; Tsinober *et al.* 2001). On the contrary, in turbulent channel flow, it is expected that the viscous contribution $\boldsymbol{a}^S$ is dominant at least in the viscous sublayer. Figure 2(*c*, *d*) shows the p.d.f.s of (a_x^I, a_x^S) and (a_y^I, a_y^S) at $y^+ = 7.8$, respectively. All p.d.f.s are normalized by the r.m.s. value of the total acceleration $\langle a_i^2 \rangle^{1/2}$. Interestingly, even in the wall region, accelerations larger than 10 r.m.s. values are mainly associated with $\boldsymbol{a}^I$. In the core of the p.d.f. ($|a^S|/\langle a^2 \rangle^{1/2} \leqslant 5$), the probability density of a_x^S is greater than a_x^I. However, a_y is determined mostly by a_y^I except in a very narrow region near the origin. It is somewhat surprising to observe that $\boldsymbol{a}^I$ is dominant even in the viscous sublayer.

3.2. *One-point statistics*

The mean streamwise A_x and wall-normal accelerations A_y normalized by the inner variables for three different Re_τ are shown in figure 3(*a*, *b*). The negative peak of A_x appears at $y^+ \simeq 7$ regardless of Re_τ. From the mean momentum equation for the streamwise velocity,

$$A_x = -1 + \frac{1}{Re_\tau} \frac{\mathrm{d}^2 U}{\mathrm{d}y^2}, \tag{3.1}$$

it is obvious that the negative peak of A_x is due to the viscous contribution. Since the mean wall-normal velocity is zero, A_y is solely determined by the irrotational acceleration. The peak A_y is observed at $y^+ \simeq 20$. Moser *et al.* (1999) have shown that the Reynolds stresses scaled by the inner variables are insensitive to the Reynolds number once $Re_\tau \geqslant 400$. Because A_x and A_y are, respectively, wall-normal gradients of $\langle uv \rangle$ and $\langle v^2 \rangle$, A_x and A_y at $Re_\tau = 408$ are almost indistinguishable from those at $Re_\tau = 600$ for $y^+ \leqslant 100$.

Figure 3(*c*, *d*) shows the r.m.s. values of a_x and a_y scaled by the inner variables. We compared the present results with the experimental data in Gerashchenko *et al.* (2008) for the Reynolds number based on u_τ and the boundary layer thickness $Re_\delta = 470$. Because they measured acceleration of finite-sized inertial particles, it is difficult to compare the results directly. However, considering the differences in physical parameters, the qualitative agreement in the r.m.s. acceleration profiles is quite satisfactory.

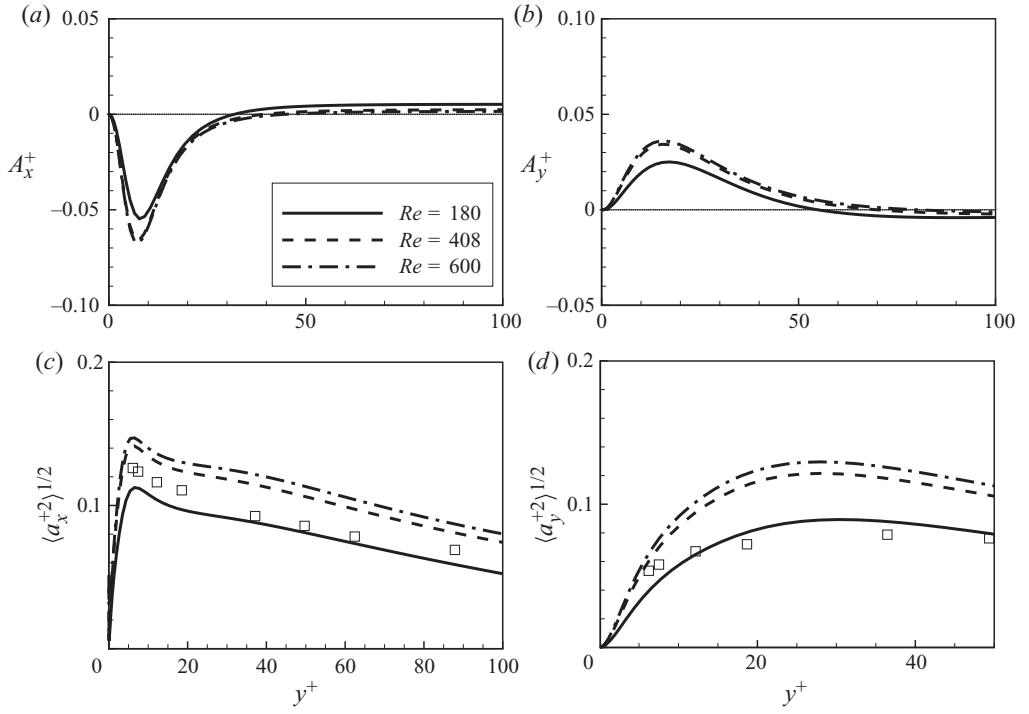

FIGURE 3. Mean and r.m.s. accelerations normalized by u_τ and δ: (*a*) mean streamwise acceleration, (*b*) mean wall-normal acceleration, (*c*) r.m.s. streamwise acceleration and (*d*) r.m.s. wall-normal acceleration in wall coordinates. □, experiments by Gerashchenko *et al.* (2008).

In figure 3(*c*, *d*), it is shown that the location of the peak $\langle a_x^2\rangle^{1/2}$ coincides with that of A_x. Unlike the mean values, the r.m.s. accelerations are shown to be increasing functions of Re_τ. However, in the viscous sublayer $y^+ \leqslant 7$, both the steamwise and wall-normal accelerations are scaled well with the inner variables when $Re_\tau \geqslant 408$. Except near the location of the peak A_i, the mean accelerations are very small compared to their r.m.s. values. At the locations of peak A_x and A_y, $\langle a_x^2\rangle^{1/2}/A_x > 2$ and $\langle a_y^2\rangle^{1/2}/A_y > 3$, in the range of Re_τ in the present simulations.

To investigate the behaviour in detail, we compute the r.m.s. values of total, irrotational and solenoidal accelerations separately for $Re_\tau = 180$ (figure 4*a*). The peaks of a_y and a_z appear in the buffer layer, where the distinguishing turbulent coherent structure of near-wall turbulence, the streamwise vortex, is observed. On the other hand, a_x reaches its maximum very near the wall, $y^+ \simeq 7$. It is shown that a_x^S is responsible for the peak a_x near the wall. The contribution of a_x^S to a_x is greater than that of a_x^I until $y^+ \simeq 20$ and the relative magnitude $|a_x^S|/|a_x^I|$ decreases slowly outwards. It is also found that $\langle a_y^{S2}\rangle$ and $\langle a_z^{S2}\rangle$ are negligibly small compared to their irrotational counterparts.

The skewness factor of a_y (S_y) is shown in figure 4(*b*). It is shown that S_y reaches its positive peak at $y^+ \simeq 7.8$ and crosses zero at $y^+ \simeq 20$. This behaviour may suggest the relation between acceleration and a turbulent coherent structure. Kim, Moin & Moser (1987) have shown that the averaged centre of the streamwise vortices is located at $y^+ \simeq 20$ with the averaged radius of $r^+ \simeq 15$. Because accelerations tend to be directed towards the core of a vortex (Lee *et al.* 2004; Lee & Lee 2005), the

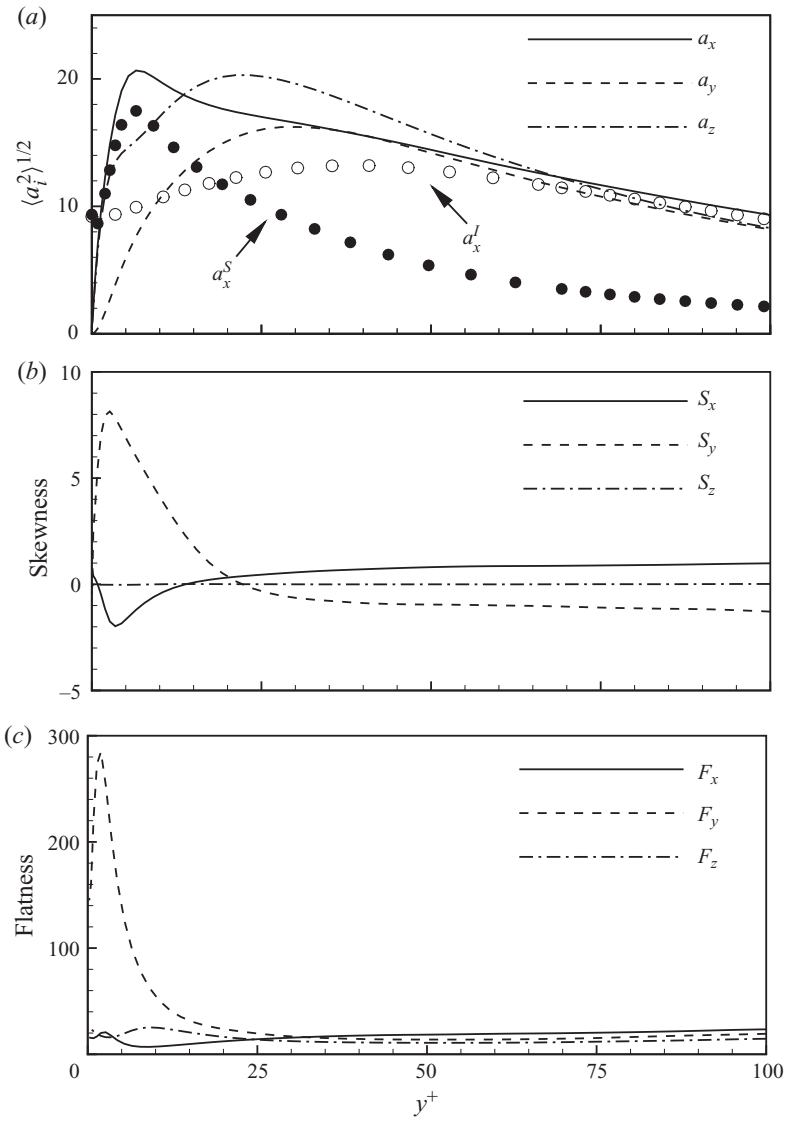

FIGURE 4. Acceleration statistics for $Re_\tau = 180$ as a function of y^+: (*a*) r.m.s. values of total, irrotational and solenoidal accelerations scaled by the wall units, (*b*) skewness and (*c*) flatness factors.

upward acceleration appearing below the vortex contributes to the positive S_y when $y^+ < 20$. Likewise, the negative S_y may be related to the downward acceleration above the streamwise vortex.

The flatness factors are presented in figure 4(*c*). The flatness factors are evaluated with about 4.7×10^9 samples to ensure convergence. The flatness factor of a_y (F_y) shows an extremely large peak in the viscous sublayer, larger than 280. The large F_y in the wall-region is due to the long positive tail of the a_y p.d.f. shown in figure 1(*a*). A close investigation of flow fields reveals that the streamwise vortices are extended from the buffer layer to the viscous sublayer causing very large upward acceleration in the viscous sublayer, which contributes to the large F_y near the wall.

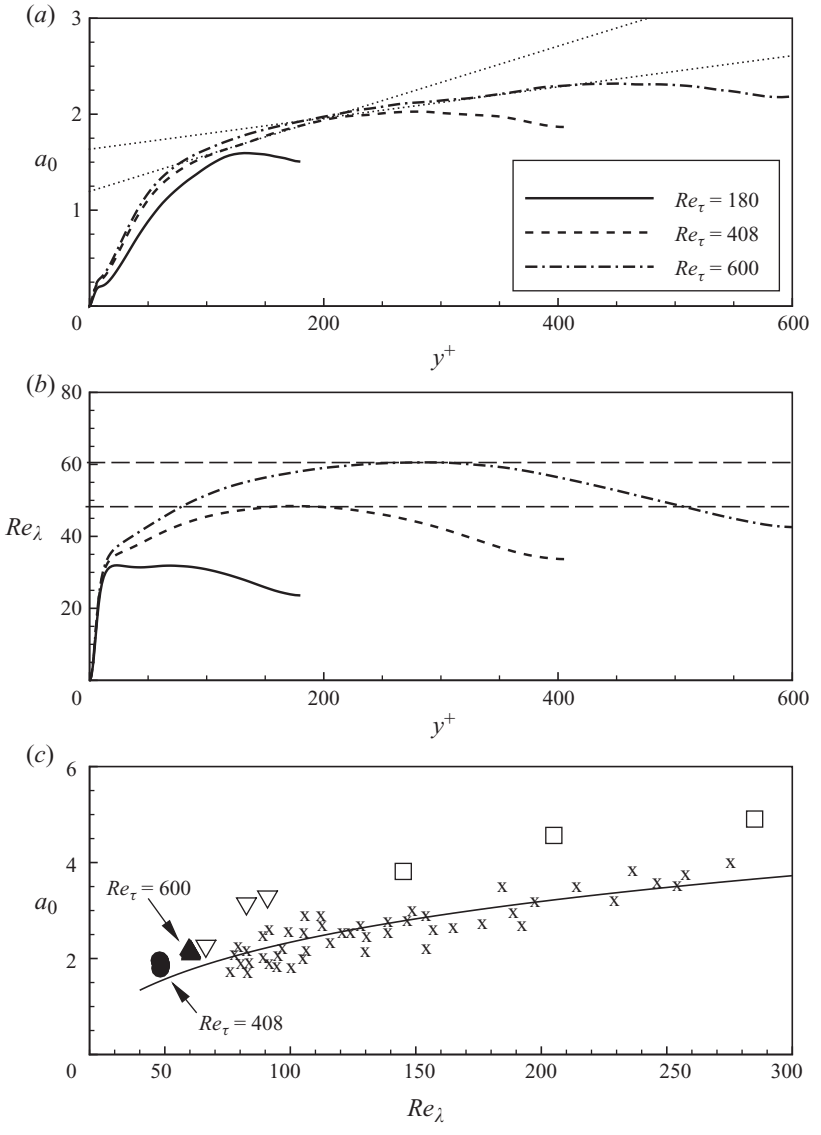

FIGURE 5. (*a*) The acceleration variance normalized by the Heisenberg–Yaglom scaling a_0 and (*b*) Taylor-scale Reynolds number Re_λ as function of y^+ for three different Re_τ. (*c*) a_0 as a function of Re_λ: ●, $Re_\tau = 408$; ▲, $Re_\tau = 600$; ×, Vedula & Yeung (1999); ▽, Lüthi *et al.* (2005); □, Voth *et al.* (2002); ———, Yeung *et al.* (2006).

3.3. *Reynolds number dependence of acceleration statistics*

The acceleration variance normalized by the Heisenberg–Yaglom scaling (Monin & Yaglom 1975) is defined as

$$a_0 \equiv \frac{1}{3}\frac{\langle \boldsymbol{a}\cdot\boldsymbol{a}\rangle}{\epsilon^{3/2}\nu^{-1/2}}, \tag{3.2}$$

in which ϵ is the dissipation rate. Figure 5(*a*) shows a_0 as a function of y^+. It is shown that a_0 is a non-decreasing function of Re_τ near the wall. In the viscous sublayer ($y^+ \leqslant 10$), a_0 collapses well for the two-higher Re_τ due to the universal

characteristic of the solenoidal acceleration (Vedula & Yeung 1999). Interestingly, a_0 is a linear function of y^+ in the log layer for $Re_\tau \geqslant 408$. The fitting curves are $a_0 = 1.20 + 3.78 \times 10^{-3} y^+$ and $a_0 = 1.64 + 1.63 \times 10^{-3} y^+$ for $Re_\tau = 408$ and 600, respectively. The slope of the fitting curve decreases significantly as Re_τ increases.

To compare a_0 with the previous results for isotropic turbulence, we estimate the Taylor-scale Reynolds number as a function of y^+. The Taylor-scale Reynolds number in inhomogeneous turbulence is estimated by $Re_\lambda = (20k^{+2}/3\epsilon^+)^{1/2}$, in which k^+ is the turbulent kinetic energy scaled by the inner variables. Figure 5(*b*) shows Re_λ profiles for different Re_τ. For $Re_\tau = 180$, Re_λ shows a local peak in the buffer layer and slowly decreases afterwards. On the other hand, plateaus are observed in the log layer at $Re_\tau = 408$ and 600.

In figure 5(*c*), we compare a_0 at the plateaus for $Re_\tau = 408$ and 600 with the previous numerical (Vedula & Yeung 1999) and experimental results (Voth *et al.* 2002; Lüthi, Tsinober & Kinzelbach 2005). In the experiments by Voth *et al.* (2002), a_0 for axial and lateral accelerations do not coincide at low Re_λ. In figure 5(*c*), we show the average of the axial and lateral a_0. The results by Vedula & Yeung (1999) is obtained from Gylfason, Ayyalasomayajula & Warhaft (2004). According to the classical Kolmogorov scaling, a_0 may show a universal behaviour at sufficiently high a_0. However, it has been observed that a_0 shows a Reynolds number dependence even at $Re_\lambda \sim 10^4$ (Gulitski *et al.* 2007). Yeung *et al.* (2006) provided an empirical fitting curve for a_0,

$$a_0 = \frac{1.3}{Re_\lambda^{0.22}} + 0.88 Re_\lambda^{0.66} \ln\left(\frac{Re_\lambda}{20}\right). \tag{3.3}$$

It is interesting to observe that a_0 estimated at the plateau of Re_λ shows a good agreement with the previous results in isotropic turbulence. From figure 5(*a*, *b*), it seems that, at higher Re_τ, there will be a region in which both Re_λ and a_0 reach plateaus and a_0 may be estimated from the data in isotropic turbulence.

Figure 6(*a*, *b*) shows the a_y skewness and flatness factors for three different Re_τ. In isotropic turbulence, it has been shown that the acceleration flatness factor is an increasing function of Re_λ. In the DNS study of Yeung *et al.* (2006), the acceleration flatness factor increases from 7 at $Re_\lambda = 7$ to 107 at $Re_\lambda = 680$. On the contrary, it is found that, near the wall ($10 < y^+ < 100$), the acceleration skewness and flatness factors are relatively less sensitive to the Reynolds numbers except in the viscous sublayer. In the viscous sublayer, both the skewness and flatness factors are increasing functions of Re_τ.

4. Behaviour of accelerations around vortices

4.1. *Alignment of accelerations with vortices*

In a vortex, pressure has its local minimum on the axis of the swirling motion because the centrifugal force is balanced by pressure gradient (Jeong *et al.* 1997). As the major contribution to acceleration comes from the pressure gradient, it is natural that acceleration is directed towards the core of a vortex. A strong correlation between a streamwise vortex and pressure gradient was first noticed by Kim (1989) in turbulent channel flow, in which he found elongated structures of $\partial p/\partial y$ and $\partial p/\partial z$ in the streamwise direction and a strong correlation between $\partial p/\partial z$ and streamwise vorticity at the wall. By investigating the acceleration–enstrophy cross-correlation function in isotropic turbulence, Yeung & Pope (1989) suggested that the fluid particles are accelerated towards regions of high vorticity. La Porta *et al.*

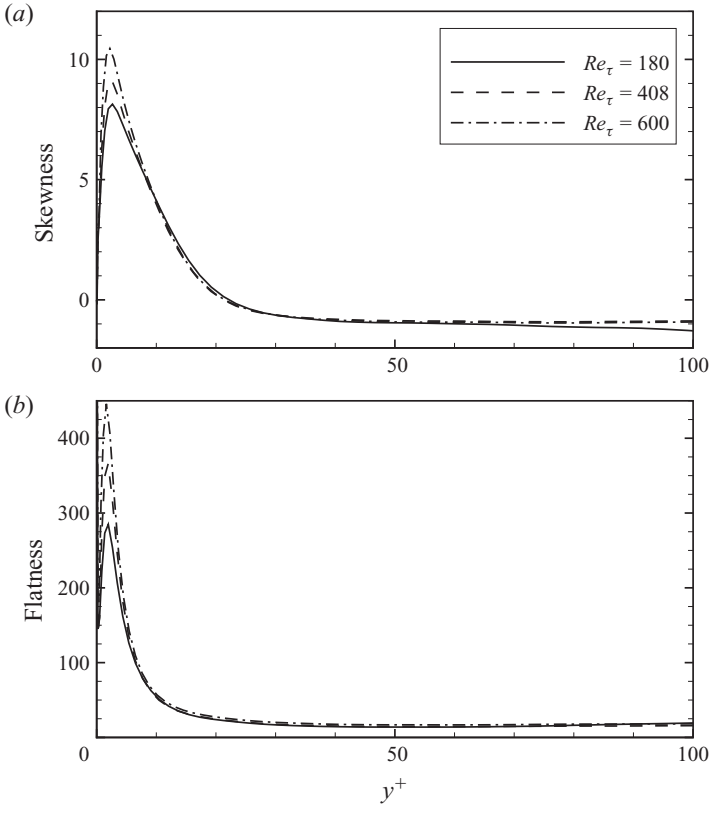

FIGURE 6. Acceleration (a) skewness and (b) flatness factors for three different Re_τ.

(2001) observed that intermittent accelerations are associated with spiral motion of fluid particles around vortices. Based on the results, Mordant *et al.* (2002) suggested that the slowly decaying Lagrangian correlation of acceleration magnitude is closely associated with the intermittency. Later, Lee *et al.* (2004) confirmed that the long-time correlation of acceleration magnitude is due to the centripetal acceleration of fluid particles trapped in a vortex.

To investigate the behaviour of acceleration near vortices quantitatively, we investigate the angles between accelerations and the gradient of squared vorticity known as the enstrophy $\boldsymbol{\omega}\cdot\boldsymbol{\omega}$, in which $\boldsymbol{\omega}$ is the fluctuating component of vorticity. We define the angle between $\boldsymbol{a}$ and $\nabla(\boldsymbol{\omega}\cdot\boldsymbol{\omega})$ as

$$\alpha = \cos^{-1}\left(\frac{\boldsymbol{a}\cdot\nabla(\boldsymbol{\omega}\cdot\boldsymbol{\omega})}{|\boldsymbol{a}||\nabla(\boldsymbol{\omega}\cdot\boldsymbol{\omega})|}\right). \tag{4.1}$$

A region of high $\boldsymbol{\omega}\cdot\boldsymbol{\omega}$ is strongly correlated with solid-body rotation of fluid and, hence, vortex tubes (Ruetsch & Maxey 1992; Blackburn, Mansour & Cantwell 1996). Since, near a vortex tube, $\boldsymbol{\omega}\cdot\boldsymbol{\omega}$ has a local maximum along the axis of the vortex and decreases radially, $\nabla(\boldsymbol{\omega}\cdot\boldsymbol{\omega})$ is perpendicular to the vortex axis.

Figure 7(a, b) illustrates the p.d.f.s of α, $P(\alpha)$. In the viscous sublayer, $P(\alpha)$, $P(\alpha^I)$ and $P(\alpha^S)$ show peaks around 90°. Because the direction of irrotational acceleration near a vortex converges into the core of the vortex, the peak of $P(\alpha^I)$ at 90° is not an expected result. Even in the buffer layer (figure 7b), $P(\alpha^I)$ does not show a

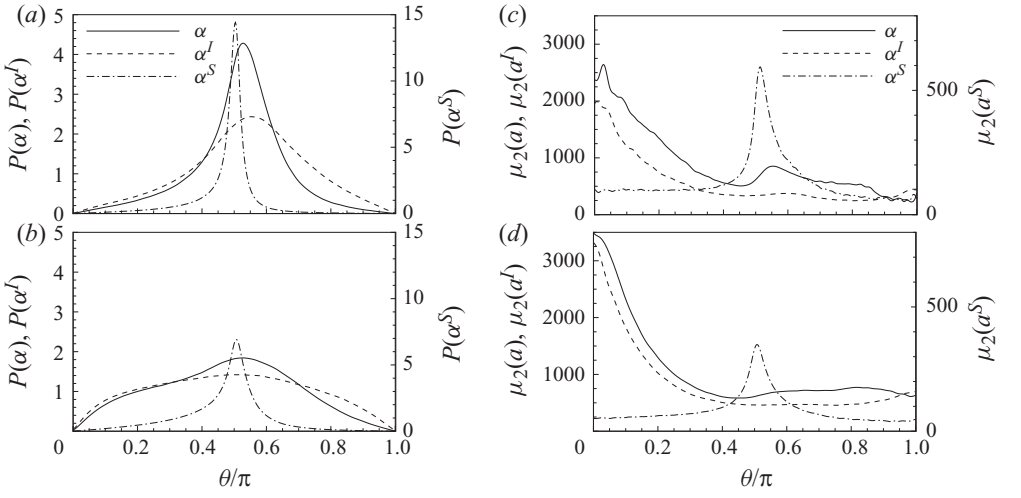

FIGURE 7. (*a*, *b*) Probability density functions of angles between $\nabla(\boldsymbol{\omega}\cdot\boldsymbol{\omega})$ and $\boldsymbol{a}$ (α), $\boldsymbol{a}^I$ (α^I) and $\boldsymbol{a}^S$ (α^S) at $y^+ = 7.8$ and $y^+ = 19.8$, respectively. (*c*, *d*) The conditional second moments of acceleration, $\mu_2(a|\alpha)$, $\mu_2(a^I|\alpha^I)$ and $\mu_2(a^S|\alpha^S)$ at $y^+ = 7.8$ and at $y^+ = 19.8$, respectively. The results are obtained at $Re_\tau = 180$.

preferential alignment with the enstrophy gradient. $P(\alpha)$ has a weak peak at $\alpha = 90^\circ$ in the buffer layer. $\boldsymbol{a}^S$ is perpendicular to the enstrophy gradient regardless of the distances from the wall. The weak peak of $P(\alpha)$ observed in the buffer layer seems to be associated with the non-negligible contribution of a_x^S to $\langle a_x^2\rangle^{1/2}$ (figure 4*a*).

The intermittent accelerations, more than 20 times larger than r.m.s. acceleration, are typically observed around vortical structures (Lee *et al.* 2004; Lee & Lee 2005). To consider the intermittent events, we computed the conditional acceleration variances, $\mu_2(a|\alpha) = \langle(\boldsymbol{a}\cdot\boldsymbol{a})|\alpha\rangle$. Figure 7(*c*, *d*) shows that the large-magnitude events of $\boldsymbol{a}$ and $\boldsymbol{a}^I$ are always aligned with the enstrophy gradient, implying that a major source of the intermittently large accelerations is centripetal accelerations near vortices. On the other hand, $\mu_2(a^S|\alpha^S)$ shows a peak at $\alpha^S = 90^\circ$ regardless of the wall distances. This behaviour of the solenoidal acceleration is explained in § 4.2. It is also observed that the acceleration events of magnitudes similar to the mean accelerations show no directional preference to the enstrophy gradient.

4.2. *Acceleration fields near the wall*

Figure 8(*a–c*) shows acceleration fields near a streamwise vortex rotating clockwise. The vortex structure is identified by the λ_2 method proposed by Jeong & Hussain (1995). It is shown that (a_y, a_z) are almost indistinguishable from (a_y^I, a_z^I), while there are some differences in the x-components (contours) due to non-negligible contribution of a_x^S to a_x. In figure 8(*a*), large positive and negative a_x are observed above and below the vortex, respectively. $\boldsymbol{a}^S$ rotates around the vortex in the counter-clockwise direction while the vortex rotates clockwise (figure 8*c*). Note that the magnitude of the reference vectors in figure 8(*c*) is different from figure 8(*a*, *b*), because the magnitudes of (a_y^S, a_z^S) are much smaller than the total and irrotational accelerations. From the Navier–Stokes equations, the relation between solenoidal acceleration and vorticity is given by

$$\nabla \times \boldsymbol{a}^S = \nu\nabla^2\boldsymbol{\omega}. \tag{4.2}$$

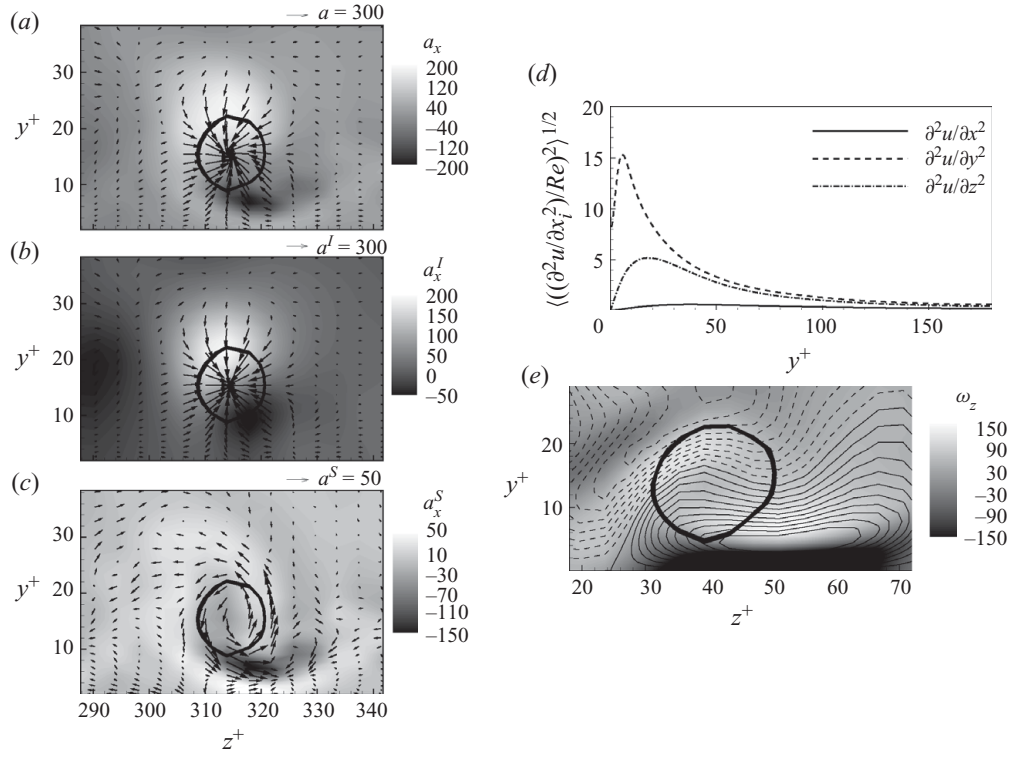

FIGURE 8. (*a–c*) Display of $\boldsymbol{a}$, $\boldsymbol{a}^I$ and $\boldsymbol{a}^S$ fields around a vortex structure. Solid line denotes the boundary of a streamwise vortex rotating clockwise. Shading shows the streamwise components of each acceleration. (*d*) Root-mean-square values of $\nu\partial^2 u/\partial x_i^2$. (*e*) High- and low-speed streaks and ω_z field around a streamwise vortex in buffer layer. Grey shading denotes ω_z. The solid and dashed lines represent positive and negative u, respectively.

In a simple one-dimensional vortex tube, the vorticity has a local maximum along the axis and decreases radially and the sign of the right-hand side of (4.2) is always opposite to the sign of $\boldsymbol{\omega}$. Hence, it can be deduced that a_y^S and a_z^S always counter-rotate with respect to the motion of the streamwise vortex. Because of the counter-rotating nature of $\boldsymbol{a}^S$, the p.d.f.s of the angle between $\boldsymbol{a}^S$ and $\nabla(\boldsymbol{\omega}\cdot\boldsymbol{\omega})$ show a peak at $\alpha^s = 90^\circ$ (figure 7*a*, *b*).

It is seen in figure 8 that the positive a_x above a vortex resembles a_x^I while the negative one below the vortex is determined by a_x^S. The positive and negative a_x^I, displayed in figure 8(*b*), are induced by the streamwise vortex which is inclined in the wall-normal direction (Lee *et al.* 2004). Typically, the large negative a_x^S occurs below the vortex, forming a sheet-like structure (figure 8*c*). It seems that the sheet-like structure contributes to the peak r.m.s. a_x^S found in the viscous sublayer (figure 3*a*). It is noteworthy to observe that the magnitude of a_x^S under the streamwise vortex is about 150 while A_x^S is about 10 in this region. a_x^S consists of three components,

$$a_x^S = \nu\left(\frac{\partial^2 u}{\partial x^2} + \frac{\partial^2 u}{\partial y^2} + \frac{\partial^2 u}{\partial z^2}\right). \tag{4.3}$$

Root-mean-square values of each component are presented in figure 8(*d*) showing that $\partial^2 u/\partial y^2$ is a major source of a_x^S near the wall. Furthermore, $|\partial v/\partial x| \ll |\partial u/\partial y|$, near the streamwise vortex. Hence, near the vortex, a_x^S may be approximated by

$\partial\omega_z/\partial y$. Jeong *et al.* (1997) have shown that high- and low-shear regions result from the streamwise vortex near the wall and ω_z changes its sign in the high-shear region. Figure 8(*e*) shows the distribution of ω_z near the streamwise vortex rotating clockwise. Below the vortex, there is a region in which ω_z changes rapidly from positive to negative and the region coincides with the location of a high-speed streak. Comparing figures 8(*c*) and 8(*e*), it seems that the sheet-like structure of a_x^S in the viscous sublayer is induced by the large $\partial\omega_z/\partial y$ below the streamwise vortex. The peak of r.m.s. a_x^S in the viscous sublayer is a consequence of the shear zone induced by the streamwise vortex.

5. Conclusions

To investigate the characteristics of acceleration in near-wall turbulent flows, DNS of turbulent channel flow were performed at $Re_\tau = 180$, 408 and 600. The fluid-particle acceleration is evaluated by summing the pressure-gradient (irrotational acceleration) and viscous forces (solenoidal acceleration).

It is shown that the acceleration field becomes more intermittent near the wall. Particularly, the p.d.f. of the wall-normal acceleration in the viscous sublayer shows extreme events, $a_y \simeq 50\langle a_y^2\rangle^{1/2}$, with the probability of 10^{-7}. In the viscous layer, the a_y flatness factor becomes $O(100)$. It is shown that such an intermittent event is governed by the irrotational acceleration, which is linked to vortical structures. The acceleration variances conditioned on the angle between the acceleration and the enstrophy gradient indicate that a vortex structure is an important source of the acceleration intermittency even in the viscous sublayer. In the viscous sublayer, the unconditioned low-order statistics, such as mean and variances, of $\boldsymbol{a}$ are largely due to $\boldsymbol{a}^S$, while intermittent events mainly come from the irrotational accelerations associated with streamwise vortices in the buffer layer. It is shown that, unlike the previous results in isotropic turbulence, the acceleration flatness and skewness factors are not sensitive to Re_τ in the buffer and log layers ($10 < y^+ < 100$).

In isotropic turbulence, $\boldsymbol{a}^S$ is negligible compared to $\boldsymbol{a}^I$. However, in near-wall turbulence, the contribution from the steamwise solenoidal acceleration is non-negligible at least in the low-order statistics of a_x, while a_y and a_z are governed by the irrotational accelerations. Visualization of acceleration fields near a vortex shows that $\boldsymbol{a}^I$ is directed towards the core of a vortex while $\boldsymbol{a}^S$ counter-rotates with respect to the motion of the vortex. It is found that the streamwise vortex is responsible not only for the intermittent characteristics of irrotational acceleration but also for the large streamwise solenoidal accelerations observed in the viscous sublayer. Below a streamwise vortex, there is a high-shear region in which a steep gradient of the spanwise vorticity $|\partial\omega_z/\partial y|$ is observed. The sheet-like structure of strong negative a_x^S is induced by the large $|\partial\omega_z/\partial y|$. The magnitude of a_x^S in this region is comparable to a_x^I in the viscous layer. It is interesting to observe that the location of the large negative a_x^S coincides with the location of a high-speed streak, indicating that the solenoidal acceleration acts to decelerate high-momentum fluid from the buffer layer to the viscous layer by the sweep events.

The Reynolds number behaviour of the acceleration Kolmogorov constant a_0 is investigated. It is found that a_0 is a linear function of y^+ in the log layer when $Re_\tau \geqslant 408$. The slope of the fitting curve is a decreasing function of Re_τ, implying that at sufficiently high Re_τ there may be a region in the log layer in which a_0 is a constant. The Taylor-scale Reynolds number reaches a plateau in the log layer for

$Re_\tau \leqslant 408$. The value of a_0 in the plateau is compared with the previous numerical and experimental data in isotropic turbulence.

We thank Dr Sreenivasan for helpful comments. This research was supported by WCU (World Class University) programme through the National Research Foundation of Korea (NRF) funded by the Ministry of Education, Science and Technology R31-2008-000-10049-0. Most computations were carried out in KISTI Supercomputing Center.

REFERENCES

Biferale, L., Boffetta, G., Celani, A., Devenish, B. J., Lanotte, A. & Toschi, F. 2004 Multifractal statistics of Lagrangian velocity and acceleration in turbulence. *Phys. Rev. Lett.* **93**, 064502.

Blackburn, H. M., Mansour, N. N. & Cantwell, B. J. 1996 Topology of fine-sacle motions in turbulent channel flow. *J. Fluid Mech.* **310**, 269–292.

Brooke, J. W., Kontomaris, K., Hanratty, T. J. & McLaughlin, J. B. 1992 Turbulent deposition and trapping of aerosols at a wall. *Phys. Fluids* A **4**, 825–834.

Calzavarnini, E., Volk, R., Bourgoin, M., Lévêque, E., Pinton, J.-F. & Toschi, F. 2009 Acceleration statistics of finite-sized particles in turbulent flow: the role of Faxén forces. *J. Fluid Mech.* **630**, 179–189.

Gerashchenko, S., Sharp, N. S., Neuscamman, S. & Warhaft, Z. 2008 Lagrangian measurements of inertial particle accelerations in a turbulent boundary layer. *J. Fluid Mech.* **617**, 255–281.

Gotoh, R. & Rogallo, R. S. 1999 Intermittency and scaling of pressure at small scales in forced isotropic turbulence. *J. Fluid Mech.* **396**, 257–285.

Gulitski, G., Kholmyansky, M., Kinzelbach, W., Lüthi, B., Tsinober, A. & Yorish, S. 2007 Velocity and temperature derivatives in high-Reynolds-number turbulent flows in the atmospheric surface layer. Part 2. Accelerations and related matters. *J. Fluid Mech.* **589**, 83–102.

Gylfason, A., Ayyalasomayajula, S. & Warhaft, Z. 2004 Intermittency, pressure and acceleration statistics from hot-wire measurements in wind-tunnel turbulence. *J. Fluid Mech.* **501**, 213–229.

Hill, R. J. 2002 Scaling of acceleration in locally isotropic turbulence. *J. Fluid Mech.* **452**, 361–370.

Hill, R. J. & Thoroddsen, S.T. 1997 Experimental evaluation of acceleration correlations for locally isotropic turbulence. *Phys. Rev.* E **55**, 1600–1606.

Jeong, J. & Hussain, F. 1995 On the identification of a vortex. *J. Fluid Mech.* **285**, 69–94.

Jeong, J., Hussain, F., Schoppa, W. & Kim, J. 1997 Coherent structures near the wall in a turbulent channel flow. *J. Fluid Mech* **332**, 185–214.

Kim, J. 1989 On the structure of pressure fluctuations in simulated turbulent channel flow. *J. Fluid Mech.* **205**, 421–451.

Kim, J., Moin, P. & Moser, R. 1987 Turbulence statistics in fully developed channel flow at low Reynolds number. *J. Fluid Mech.* **177**, 133–166.

La Porta, A., Voth, G. A., Crawford, A. M., Alexander, J. & Bodenschatz, E. 2001 Fluid-particle accelerations in fully developed turbulence. *Nature* **409**, 1017–1019.

Lee, S. & Lee, C. 2005 Intermittency of acceleration in isotropic turbulence. *Phys. Rev.* E **71**, 056310.

Lee, C., Yeo, K. & Choi, J.-I. 2004 Intermittent nature of acceleration in near-wall turbulence. *Phys. Rev. Lett.* **92**, 144502.

Lundbladh, A., Berlin, S., Skote, M., Hildings, C., Choi, J., Kim, J. & Henningson, D. S. 1999 An efficient spectral method for simulation of incompressible flow over a flat plate. *Tech. Rep.* 1999:11. Royal Institute of Technology, Stockholm.

Lüthi, B., Tsinober, A. & Kinzelbach, W. 2005 Lagrangian measurement of vorticity dynamics in turbulent flow. *J. Fluid Mech.* **528**, 87–118.

Monin, A. S. & Yaglom, A. M. 1975 *Statistical Fluid Mechanics*, vol. 2. MIT Press.

Mordant, N., Delour, J., Léveque, E., Arnéodo, A. & Pinton, J.-F. 2002 Long time correlations in Lagrangian dynamics: a key to intermittency in turbulence. *Phys. Rev. Lett.* **89**, 254502.

Moser, R. D., Kim, J. & Mansour, N. N. 1999 Direct numerical simulation of turbulent channel flow up to $Re_\tau = 590$. *Phys. Fluids* **11**, 943–945.

Pope, S.B. 1994 Lagrangian PDF methods for turbulent flows. *Annu. Rev. Fluid Mech.* **26**, 23–63.

Qureshi, N. M., Bourgoin, M., Baudet, C., Cartellier, A. & Gagne, Y. 2007 Trubulent transport of material particles: an experimental study of finite size effects. *Phys. Rev. Lett.* **99**, 184502.

Reynolds, A. M. 1999 A second-order Lagrangian stochastic model for particle trajectories in inhomogeneous turbulence. *Q. J. R. Meteorol. Soc.* **125**, 1735–1746.

Ruetsch, G. R. & Maxey, M. R. 1992 The evolution of small-scale structures in homogeneous isotropic turbulence. *Phys. Fluids* A **4**, 2747–2760.

Sawford, B. L. 1991 Reynolds number effects in Lagrangian stochastic models of turbulent dispersion. *Phys. Fluids* A **3**, 1577–1586.

Setyawan, H., Shimada, M., Ohtsuka, K. & Okuyama, K. 2002 Visualization and numerical simulation of fine particle transport in a low-pressure parallel plate chemical vapor deposition reactor. *Chem. Engng Sci.* **57**, 497–506.

Toschi, F. & Bodenschatz, E. 2009 Lagrangian properties of particles in turbulence. *Annu. Rev. Fluid Mech.* **41**, 375–404.

Tsinober, A., Vedula, P. & Yeung, P. K. 2001 Random Taylor hypothesis and the behavior of local and convective accelerations in isotropic turbulence. *Phys. Fluids* **13**, 1974–1984.

Vedula, P. & Yeung, P. K. 1999 Similarity scaling of acceleration and pressure statistics in numerical simulations of isotropic turbulence. *Phys. Fluids* **11**, 1208–1200.

Volk, R., Calzavarnini, E., Verhille, G., Lohse, D., Mordant, N., Pinton, J.-F. & Toschi, F. 2008 Acceleration of heavy and light particles in turbulence: comparison between experiments and direct numerical simulations. *Physica* D **237**, 2084–2089.

Voth, G. A., La Porta, A., Crawford, A. M., Alexander, J. & Bodenschatz, E. 2002 Measurement of particle accelerations in fully developed turbulence. *J. Fluid Mech.* **469**, 121–160.

Yeo, K., Dong, S., Climent, E. & Maxey, M. R. 2010 Modulation of homogeneous turbulence seeded with finite size bubbles or particles. *Intl J. Multiph. Flow* **36**, 221–233.

Yeo, K., Kim, B.-G. & Lee, C. 2009 Eulerian and Lagrangian statistics in stably stratified turbulent channel flows. *J. Turbul.* **10**, 17.

Yeung, P. K. 1997 One- and two-particle Lagrangian acceleration correlations in numerically simulated homogeneous turbulence. *Phys. Fluids* **9**, 2981–2990.

Yeung, P. K. & Pope, S. B. 1989 Lagrangian statistics from direct numerical simulations of isotropic turbulence. *J. Fluid Mech.* **207**, 531–586.

Yeung, P. K., Pope, S. B., Kurth, E. A. & Lamorgese, A. G. 2007 Lagrangian conditional statics, acceleration and local relative motion in numerically simulated isotropic turbulence. *J. Fluid Mech.* **582**, 399–422.

Yeung, P. K., Pope, S. B., Lamorgese, A. G. & Donzis, D. A. 2006 Acceleration and dissipation statistics of numerically simulated isotropic turbulence. *Phys. Fluids* **18**, 065103.